



Enhanced photodegradation of toxic organic pollutants using dual-oxygen-doped porous g-C₃N₄: Mechanism exploration from both experimental and DFT studies

Sai Zhang^a, Yang Liu^a, Pengcheng Gu^a, Ran Ma^a, Tao Wen^{a,*}, Guixia Zhao^a, Lei Li^a, Yuejie Ai^{a,*}, Chun Hu^b, Xiangke Wang^{a,*}

^a MOE Key Laboratory of Resources and Environmental Systems Optimization, College of Environmental Science and Engineering, North China Electric Power University, Beijing, 102206, PR China

^b School of Environmental Sciences and Engineering, Guangzhou University, Guangzhou, 510006, PR China

ARTICLE INFO

Keywords:

Photocatalytic degradation
Graphitic carbon nitride
Dual-O-doped
Porous structure
Density functional theory

ABSTRACT

Novel visible-light-driven dual-oxygen-doped porous g-C₃N₄ (OPCN) photocatalysts were synthesized by a facile thermal copolymerization of urea and ammonium oxalate. The introduced O atoms were preferable to synchronously substitute for two sp²-hybridized N atoms in the para-positions (i.e., N1' and N4' sites) of the melem unit by forming dual-O-doped g-C₃N₄. Together with porous structures, OPCN exhibited enlarged specific surface area, narrowed band gap and expanded visible light response. The photocatalytic activity of the optimal OPCN was approximately 9 times higher than that of pure g-C₃N₄ for bisphenol A (BPA) removal under visible light irradiation, and efficient removal rates for various chlorophenols, phenols and dyes were also observed. Combined with experiments and DFT calculations, this dual-O-doped structure resulted in effective charge transfer and separation of OPCN under visible light irradiation by forming e⁻ and h⁺-related conjugated delocalized systems on the surface, which contributed to its interfacial contact with organic pollutants and adsorbed O₂. As a result, the degradation of BPA was readily induced by photoinduced h⁺ and then thoroughly mineralized by O₂^{•-}. On the other hand, more O₂^{•-} radicals were generated, which could also oxidize BPA directly due to their strong oxidation power. The superior stability and reusability of OPCN catalysts were also revealed during photoreaction. This work provides a novel viewpoint to fabricate high-performance nonmetal photocatalysts for wastewater treatment.

1. Introduction

Semiconductor-based photocatalysis has received a substantial amount of attention and has been identified as a promising “green” technique for addressing environmental pollution issues including the mineralization of organic pollutants, elimination of heavy metals and radionuclides, bacterial inactivation and NO oxidation [1–4]. To obtain inexpensive, stable and high-performance photocatalysts, thousands of functional materials have been developed, such as metal oxides/sulfides and silver halides [5–7]. Recently, graphitic carbon nitride (g-C₃N₄) has gradually become an appealing organic semiconductor in photocatalysis due to its suitable optical band gap (~2.7 eV) with visible light response, favorable thermal and chemical stability, low cost, and environmental friendliness [2,8]. Unfortunately, g-C₃N₄ nearly always suffers from inefficient visible-light utilization, poor specific surface

area, as well as high recombination and inferior mobility of photo-excited charge carriers, resulting in reduced photocatalytic performance [9,10].

Over time, continuous efforts have been devoted to enhance the photocatalytic efficiency of g-C₃N₄, such as doping heteroatoms (e.g., K [11], W [12] and S [13]), forming heterostructures with other semiconductors (e.g., TiO₂ [14], Ni₂P [15] and Ag₂CrO₄ [16]), coupling with conductive materials (e.g., reduced graphene oxide [17]) or cocatalysts (e.g., Au and Pt [18]), and fabricating various microstructures. Among these methods, the construction of porous structure can provide a large specific surface area and readily diffusion channels, which collectively enhance light harvest, accelerate mass transfer process and supply more active sites for photocatalytic reactions [19,20]. In addition, nonmetal element doping, including O [19], P [21], B [22], C [23] and S [13,24], could further effectively improve the photocatalytic

* Corresponding authors.

E-mail addresses: twen@ncepu.edu.cn (T. Wen), aiyuejie314@126.com (Y. Ai), xkwang@ncepu.edu.cn (X. Wang).

<https://doi.org/10.1016/j.apcatb.2019.02.008>

Received 12 December 2018; Received in revised form 29 January 2019; Accepted 6 February 2019

Available online 08 February 2019

0926-3373/© 2019 Elsevier B.V. All rights reserved.

performance of $g\text{-C}_3\text{N}_4$ by modifying its chemical properties and narrowing the band gap, as well as adjusting electronic structures. However, the specific substitution positions and doping modes of the introduced heteroatoms have not yet been accurately reported. Apart from these problems, the enhanced photodegradation mechanisms induced by heteroatom dopants were not elucidated clearly, which was also crucial for designing novel metal-free photocatalysts. Moreover, porous structures of heteroatom-doped $g\text{-C}_3\text{N}_4$ mostly required additional hard templates (SiO_2 [25] and SBA-15 [26], etc.) or complicated post-treatments with hazardous chemicals (H_2O_2 [27] and HNO_3 [28], etc.). Therefore, a facile and eco-friendly method to overcome those tedious processes is necessary and expected to be developed by integrating both the non-metal heteroatom doping and construction of porous structure together, especially for practical applications.

Herein, efficient visible-light dual-O-doped porous $g\text{-C}_3\text{N}_4$ (OPCN) photocatalysts were successfully synthesized by thermal copolymerization of urea and ammonium oxalate ($(\text{NH}_4)_2\text{C}_2\text{O}_4$, AO), a simple and environment-friendly method for large-scale application. Remarkably, OPCN displayed significantly enhanced photodegradation efficiency with respect to various organic pollutants and superior stability under visible light irradiation by contrast with pure $g\text{-C}_3\text{N}_4$. The morphology, chemical composition, doping behavior, optical absorption and optoelectronic properties were thoroughly characterized to explain the outstanding photodegradation behaviors of OPCN, which were derived from the synergistic interaction of porous structure and O doping after the introduction of AO. Experimental analyses together with DFT calculations explored the band structures and optimal O doping positions, further providing deep insights into the charge transfer on OPCN. The enhanced photodegradation mechanism was also postulated to better understand the impacts of heteroatom dopants on nonmetal photocatalysts.

2. Experimental section

2.1. Chemicals

All chemicals and reagents were at least analytical grade and used without further purification. The detailed information is shown in the Supporting Information (SI). Ultrapure water ($> 18.2 \text{ M}\Omega$) was used in this study.

2.2. Preparation of OPCN and pure $g\text{-C}_3\text{N}_4$

OPCN photocatalysts were synthesized by a facile thermal polymerization after the hydrothermal-assisted pretreatment of urea and $(\text{NH}_4)_2\text{C}_2\text{O}_4$. Briefly, 0.3, 0.5, 1 and 2 g of $(\text{NH}_4)_2\text{C}_2\text{O}_4$ were added into 20 mL of aqueous suspensions containing urea (10 g) and stirred at ambient temperature for 1 h. Subsequently, the mixtures were heated to 353 K to evaporate for dryness. The residual white solids were ground

into powder and calcined at 823 K for 2 h in closed ceramic crucibles with a heating rate of $5 \text{ K}\cdot\text{min}^{-1}$. Finally, the resultant products were obtained and denoted as OPCN-X ($X = 0.3, 0.5, 1, 2$), where X represents the mass of $(\text{NH}_4)_2\text{C}_2\text{O}_4$. The above calcination temperature was explored in advance by activity evaluations (Fig. S1) of the catalysts, which were synthesized via thermal polymerization at different temperatures with 1 g of $(\text{NH}_4)_2\text{C}_2\text{O}_4$ and 10 g of urea as precursors. According to the best degradation behaviors, the optimal calcination temperature was determined to be 823 K. For comparison, pure $g\text{-C}_3\text{N}_4$ was also synthesized by calcining urea directly at 823 K.

2.3. Characterization

The obtained samples were characterized by means of XRD, FTIR, FESEM, TEM, BET, XPS, EPR, ^{13}C MAS NMR and other techniques. More detailed characterization information is listed in the SI.

2.4. Computational method

Density functional theory (DFT) calculations on the slab models were carried out with Vienna *ab initio* Simulation Package (VASP) [29]. The photodegradation mechanisms of bisphenol A (BPA) over OPCN catalysts were investigated by the DFT method implemented in the Gaussian 09 package. The computational details can be found in SI.

2.5. Photocatalytic degradation experiments

The photocatalytic performances of the obtained catalysts were evaluated by degrading BPA with a 300 W Xenon lamp (CEL-HXF300, Beijing CEL Tech. Co., Ltd.) as the visible light source ($420 \text{ nm} \leq \lambda \leq 780 \text{ nm}$). The light intensity was $25 \text{ mW}\cdot\text{cm}^{-2}$, which was measured with a radiometer (Photoelectric Instrument Factory Beijing Normal University). Typically, 50 mg of photocatalysts was dispersed in 50 mL of BPA aqueous solution (20 mg L^{-1}) and magnetically stirred in the dark for 30 min to ensure an adsorption-desorption equilibrium before irradiation. Then, 2 mL of suspensions were collected for analyses at given time intervals. The BPA concentrations were measured by high-performance liquid chromatography (HPLC, Prominence-i LC-2030; Shimadzu) with a C-18 column ($5 \mu\text{m}$, $3.9 \text{ mm} \times 150 \text{ mm}$; Shimadzu) at the wavelength of 225 nm. The mobile phase was a mixture of methanol/ultrapure water (70/30%, v/v). In addition, target pollutants including phenol, 2-chlorophenol (2-CP), 2,4-dichlorophenol (2,4-DCP), 2,4,6-trichlorophenol (2,4,6-TCP), methyl orange (MO), methylene blue (MB) and rhodamine B (RhB) were also degraded. The total organic carbon (TOC) of the solution was monitored with a TOC- V_{CPH} analyzer (Shimadzu).

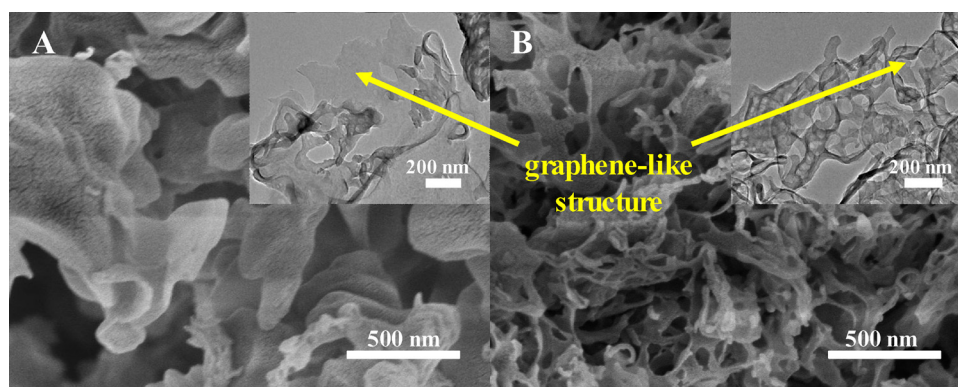


Fig. 1. FESEM images of (A) $g\text{-C}_3\text{N}_4$ and (B) OPCN-1 (the insets in Fig. 1A and B represented the corresponding TEM images).

3. Results and discussion

3.1. Characterization of OPCN

The morphologies and microstructures of different samples were observed by FESEM and TEM images. As shown in Fig. 1A, pure g-C₃N₄ displayed large bulk particles with typical stacked lamellar structure. After AO treatment, OPCN-1 revealed an irregular porous structure with ultrathin layers (Fig. 1B). TEM images (the insets in Fig. 1A and 1B) further confirmed that both samples contained graphene-like structure, and the smooth surface of g-C₃N₄ turned into the porous structure of OPCN-1, which resulted from the released gases (NH₃, H₂O, CO and CO₂) by AO decomposition during the pyrolysis process [30]. Moreover, the porous structures provided higher specific surface areas and larger pore volumes for OPCN catalysts, leading to exposure of more reactive sites. Subsequently, N₂ adsorption-desorption measurements were performed to obtain the detailed textural information of the as-prepared materials (Table S1). The BET specific surface areas were determined as 47.19 m² g^{−1} for OPCN-0.3, 52.29 m² g^{−1} for OPCN-0.5, 58.80 m² g^{−1} for OPCN-1 and 61.45 m² g^{−1} for OPCN-2, which were higher than that of pristine g-C₃N₄ (41.57 m² g^{−1}). Correspondingly, OPCN catalysts owned the larger pore volumes (0.158, 0.180, 0.185 and 0.199 cm³ g^{−1}, respectively) in contrast to g-C₃N₄ (0.129 cm³ g^{−1}). The increased BET surface areas and pore volumes were probably derived from the large amount of voids, which was well in line with the TEM and SEM images.

Fig. 2A presented the XRD patterns of g-C₃N₄ and OPCN catalysts. All samples revealed a typical g-C₃N₄ layered structure with two obvious characteristic peaks at approximately 13.1° and 27.3°, which were ascribed to (100) and (002) peaks, respectively. The stronger (002)

peak was attributed to the periodic interlayer stacking of conjugated aromatic systems, indicating the unique graphitic structure of g-C₃N₄ [12]. Furthermore, the (100) diffraction peak corresponded to the in-plane ordering of polymeric melem units [15]. Particularly, compared to g-C₃N₄, the (002) diffraction peaks of OPCN samples shifted to lower angles (from 27.3° in g-C₃N₄ to 27.0° in OPCN-1) and their intensities gradually decreased with increasing AO concentrations, indicating that the interplanar stacking distance increased and the long-range order of graphitic stacking decreased after O doping [19]. In addition, the (100) peaks became obviously weakened, which was induced by more disordered in-plane tri-s-triazine motifs in the modified catalysts resulting from the introduction of O atoms and the construction of porous structures [19]. This could be derived from incomplete molecular polymerization due to the AO pyrolysis process. Furthermore, as shown in Fig. S2, FTIR spectra of OPCN samples demonstrated the information regarding molecular structures, which were similar to that of g-C₃N₄. Broad peaks in the 3000–3600 cm^{−1} region belonged to the residual symmetric and antisymmetric stretch vibrations of N–H bonds in the surface free amino groups and O–H in absorbed H₂O molecules [20]. The strong bands ranging from 1200 to 1700 cm^{−1} and sharp peaks located at 810 cm^{−1} could be attributed to the typical stretching vibrations of aromatic C–N heterocycles and the breathing mode of tri-s-triazine units, respectively [19]. However, characteristic peaks at 810, 1246, 1416 and 1568 cm^{−1} slightly shifted to higher frequencies for OPCN samples, indicating the change of coordination environment of C–N and C=N covalent bonds. These results implied that O was successfully doped into g-C₃N₄ by covalent bonds without destroying its primary structure.

The elemental compositions and chemical states of OPCN were studied by EA and XPS, respectively. As summarized in Table 1, the C

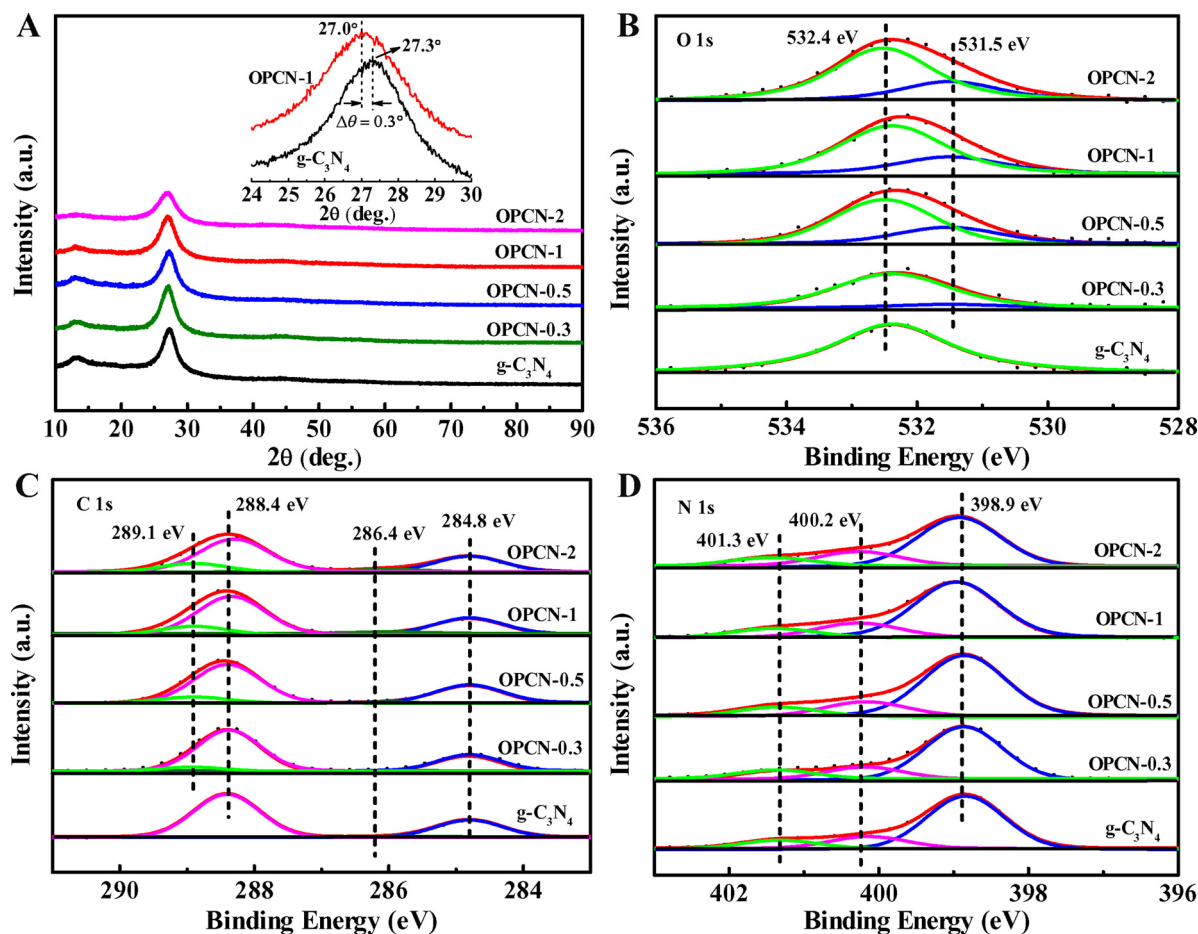


Fig. 2. (A) XRD patterns and high-resolution XPS spectra of (B) O 1s, (C) C 1s and (D) N 1s for g-C₃N₄ and OPCN samples.

Table 1
The elemental compositions of different samples.

Samples	C [wt%]	N [wt%]	O [wt%]	N/C atomic ratio	O/C atomic ratio
g-C ₃ N ₄	33.78	59.75	4.28	1.516	0.095
OPCN-0.3	33.83	59.75	4.41	1.514	0.098
OPCN-0.5	33.53	59.21	5.06	1.513	0.113
OPCN-1	33.24	57.32	7.12	1.478	0.161
OPCN-2	33.51	56.75	7.48	1.452	0.168

contents in the samples showed scarcely any change, while N/C atomic ratios decreased progressively from 1.516 to 1.452 with increasing AO usage. Contrarily, the O/C atomic ratios increased obviously from 0.095 to 0.168, implying that O atoms could substitute for N atoms by generating oxygen-containing species in matrices. To further certify the existence and true location of O atoms in the matrices of OPCN, the high-resolution spectra of O 1s, C 1s and N 1s were also recorded, as depicted in Fig. 2B, C and D, respectively. Pure g-C₃N₄ possessed the O 1s core level at 532.4 eV (O₁) belonging to surface adsorbed H₂O [31]. Interestingly, new peaks at 531.5 eV (O₂) emerged for OPCN samples, which could be ascribed to the O–C–N and O–C species formed in the lattice by O doping [28]. Meanwhile, the C 1s spectrum of g-C₃N₄ could be deconvoluted into three peaks: C₁ (284.8 eV) in surface adventitious carbon, C₂ (286.4 eV) in C–NH₂ species and C₃ (288.4 eV) in the sp²-hybridized carbon atoms of triazine rings (N–C=N) [10,19,21]. However, the new peaks appearing at 289.1 eV (C₄) confirmed the generation of O–C–N bonds in OPCN samples, implying that O atoms were directly introduced and bonded with sp²-hybridized carbons by substituting N atoms. The corresponding N 1s spectra of all samples could be separated into three peaks centered at 398.9, 400.2 and 401.3 eV, which were assigned to pyridinic nitrogen of triazine rings in C–N=C (N₁), the bridging nitrogen in N–(C)₃ (N₂) and nitrogen atoms in amino groups (C–N–H, N₃) [21,30], respectively. Furthermore, detailed XPS analyses were carried out, as recorded in Table S2. By comparison, the respective atomic ratios of O₂/O₁ and C₄/C_{total} (C_{total} = C₁ + C₂ + C₃ + C₄) increased from 0 to 0.369 and 0 to 0.151 with increasing AO usage. Nevertheless, atomic ratios of N₁/N₂, N₁/N₃ and C₃/C_{total} decreased markedly from 4.465 to 3.490, 6.178 to 5.872 and 0.707 to 0.542, respectively. The results indicated that the sp²-hybridized triazine-based structure in OPCN was gradually destroyed due to the substitution of multi-electron O atoms for N atoms by embedding into N-containing aromatic rings.

Subsequently, the hypothetical tri-s-triazine structure was verified by the solid-state ¹³C NMR technology (Fig. 3A). Both g-C₃N₄ and OPCN-1 revealed two distinct peaks located at 163.0 and 155.3 ppm, which corresponded with the C atoms of CN₃ and CN₂(NH_x) in tri-s-triazine networks, respectively [19,32]. The phenomenon proved that the characteristic poly-(tri-s-triazine) structures existed in as-obtained OPCN samples, which accorded with XRD and FTIR analyses. Fascinatingly, the peak intensity at 155.3 ppm was significantly weakened for OPCN-1, further indicating that the imperfect tri-s-triazine structure was formed due to the introduction of O atoms by substituting for N atoms, which bonded to C atoms of C–NH_x groups in the matrix. Consequently, more valence electrons in O atoms than N atoms would produce extra electrons in OPCN and redistribute to their nearest C atoms, resulting in enhancement of delocalized conjugated π system [31]. Therefore, EPR measurements were performed to determine the increased unpaired electrons on carbon atoms of the aromatic rings, as revealed in Fig. 3B. Both photocatalysts owned similar EPR signals centered at $g = 2.0036$, which was assigned to unpaired electrons on the carbon atoms of π -conjugated aromatic rings [33]. Compared with g-C₃N₄, the fairly enhanced EPR intensity of OPCN-1 in the dark or upon visible-light irradiation attested that more unpaired electrons were generated after O doping.

To investigate the optical absorption and electronic structures,

UV–vis DRS spectra of different catalysts were investigated. Fig. 3C revealed that enhanced light-harvesting capability across the whole range (200–800 nm) and remarkable bathochromic shifts of absorption edges from 450 nm to 680 nm emerged for samples with increasing AO usage. The corresponding band gaps determined from Tauc's plots (Fig. 3D) were reduced from 2.74 eV for g-C₃N₄ to 2.10, 2.05, 1.93 and 1.80 eV for OPCN-0.3, OPCN-0.5, OPCN-1 and OPCN-2, respectively. The increased optical absorption of OPCN catalysts could be considered as the result of multiple incident light reflection across porous structures and modulated electronic structures resulting from O doping, as previously mentioned [33]. Subsequently, the valence band (VB) and conduction band (CB) potentials of different photocatalysts were calculated according to the following equations:

$$E_{VB} = \chi - E_e + 0.5E_g \quad (1)$$

$$E_{CB} = E_{VB} - E_g \quad (2)$$

where E_{CB} , E_{VB} , E_g and E_e were the conduction band potential, valence band potential, band gap and the energy of free electrons on the hydrogen scale (~ 4.5 eV vs NHE), respectively [13]. χ was the electronegativity of a semiconductor; this value for g-C₃N₄ was 4.64 eV. Therefore, the E_{VB} and E_{CB} values of g-C₃N₄ were estimated to be 1.51 eV and -1.23 eV, respectively. According to the valence-band XPS spectra (Fig. S3), the negative shifts of E_{VB} emerged from 0.34 eV to 0.56 eV for OPCN catalysts in comparison with g-C₃N₄. That is, the E_{VB} of g-C₃N₄ was disturbed by the introduction of dual O atoms, and OPCN possessed lower E_{VB} than pure g-C₃N₄. Consequently, the E_{VB} values were calculated to be 1.17, 1.15, 1.06 and 0.95 eV (vs. NHE) for OPCN-0.3, OPCN-0.5, OPCN-1 and OPCN-2, respectively. According to Eq. (2), the corresponding E_{CB} values were determined to be -0.93 eV, -0.90 eV, -0.87 eV and -0.85 eV (vs. NHE), respectively. The detailed energy level diagrams of different photocatalysts were depicted in Fig. 3E. It was exhibited that the narrower band gaps and fitted energy levels of OPCN catalysts could arise from the extended delocalized π -electron system and shortened C–N bond length via O doping [19,34]. Therefore, OPCN exhibited strong optical absorption and thermodynamically derived photocatalytic oxidation of refractory organic pollutants.

First-principle simulations based on DFT were further conducted to investigate the possible O-doping positions and band structure of OPCN. According to the N/C and O/C atomic ratios in Table 1, three single- and six double- substituted models were taken into consideration by replacing the N atoms with O atoms in g-C₃N₄. As depicted in Fig. S4A, the formation energies (E) of single-substituted O atoms at N1, N2 and N3 positions were calculated to be -0.34 eV (E_1), -1.17 eV (E_2) and -0.35 eV (E_3), respectively. Therefore, we determined that the most possible substitution position for single O atom was at the N2 site, and this was consistent with the previous report [27]. Unexpectedly, much lower formation energies were obtained for disubstitution in view of all possible doping combinations. From Fig. S4B, the formation energy of double-substituted O atoms at both N1' and N4' sites was -2.66 eV ($E_1'4'$), slightly lower than in other cases, suggesting that the introduced O atoms were preferable to synchronously substitute for two sp²-hybridized N atoms in the para-positions of melem units. These results provided an in-depth proof of O doping behavior revealed by XPS, ¹³C NMR and EPR analyses; particularly, dual-O-doped g-C₃N₄ was prepared in our study.

The optimized geometries of pure g-C₃N₄ and dual-O-doped OPCN (disubstitution at N1' and N4' atoms) were shown in Fig. 4A and B, respectively. After O doping, most of the C–N bond lengths were slightly shortened by contrast with those in pure g-C₃N₄ (Table S3). To explore such geometric variation, we further calculated their density of states (DOS) and differential charge density. On one hand, a much narrower band gap energy was calculated for OPCN (1.22 eV) than for g-C₃N₄ (1.49 eV), as shown in Fig. 4C, which qualitatively corresponded to the bathochromic shift of the absorption edge mentioned above. The DFT method somehow underestimated the band gaps compared to

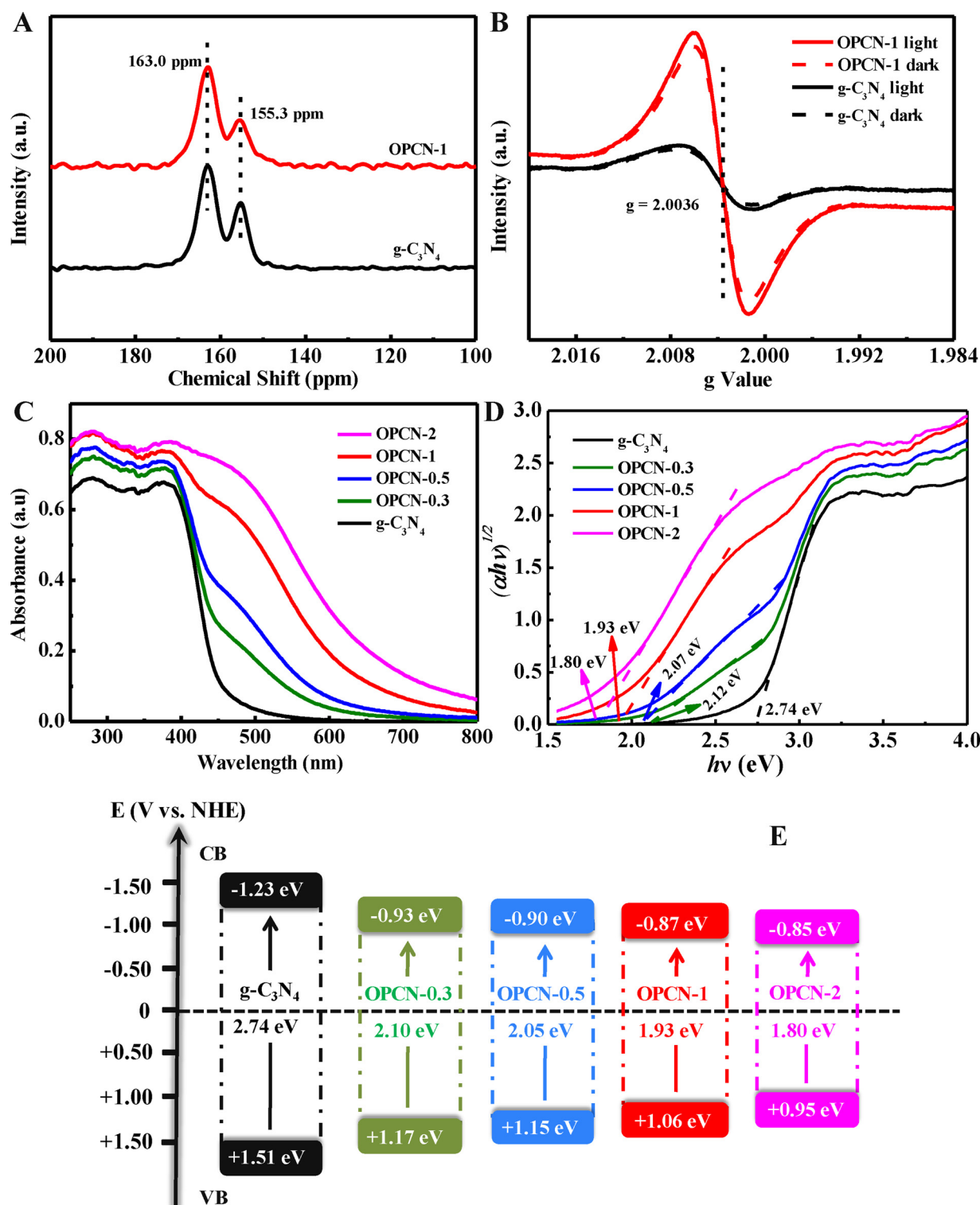


Fig. 3. (A) Solid-state ^{13}C MAS NMR spectra, (B) EPR spectra, (C) UV-vis DRS spectra, (D) the corresponding Tauc's plots and (E) schematic illustration of energy level diagrams for as-obtained catalysts.

experimental analyses [19]. On the other hand, in Fig. 4D and E, compared with $\text{g-C}_3\text{N}_4$, an obvious charge transfer was observed between doped O atoms and other atoms in aromatic heterocycles. From the above analyses, one might conclude that charge redistributions and electronic polarization were clearly located on OPCN after O doping, which was beneficial for transfer and separation of photoinduced electron-hole ($\text{e}^- - \text{h}^+$) pairs [27]. Furthermore, the charge distributions on photoexcited OPCN and $\text{g-C}_3\text{N}_4$ were recalculated with one

extra e^- or h^+ injected, respectively. Based on Bader charge analysis, upon excitation of OPCN, electrons were mainly distributed on C atoms (0.43 e^-) and N atoms (0.52 e^-), while holes only accumulated on N atoms (0.63 h^+), especially for $\text{N}2'$ (0.11 h^+), which implied that photogenerated charge carriers were separated effectively. From Fig. S5, photogenerated electrons on both $\text{g-C}_3\text{N}_4$ and OPCN mainly paralleled with their aromatic motifs by forming conjugated delocalized π systems [35]. Unexpectedly, the distribution of holes on the surface of

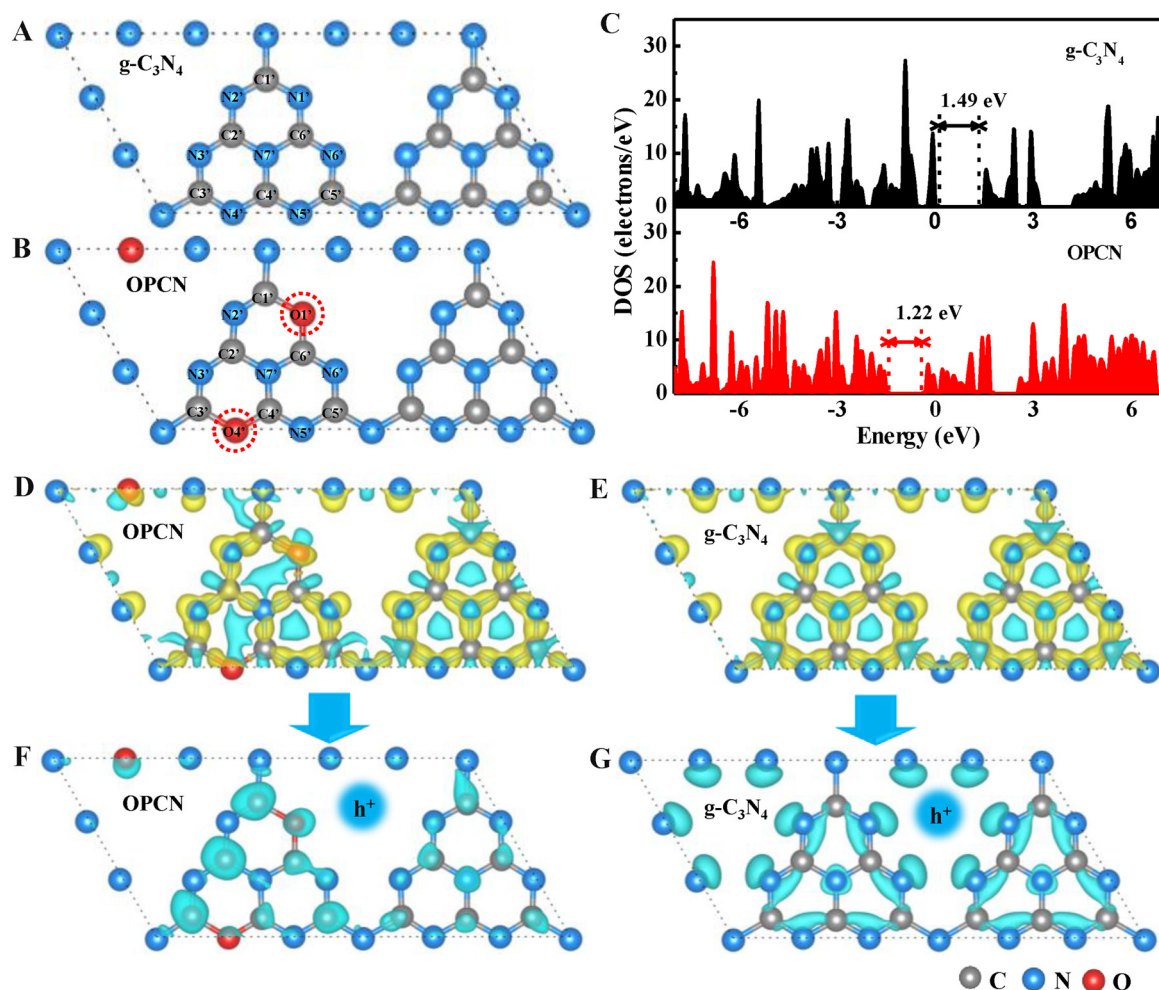


Fig. 4. (A, B) Optimized unit cells, (C) calculated DOS plots, (D, E) differential charge densities of OPCN and g-C₃N₄ models. Computed charge distributions on (F) OPCN and (G) g-C₃N₄ upon excitation by one extra hole carriers, respectively (gray, blue and red balls represented C, N and O elements, respectively) (For interpretation of the references to colour in this figure legend, the reader is referred to the web version of this article).

OPCN (Fig. 4F) was also transferred to shape a conjugated structure by comparison with g-C₃N₄ (Fig. 4G), on which holes were along the direction of in-plane lone pair electrons in N atoms. As a result, the surface charge density and delocalized conjugated systems were expanded, which could accelerate charge carriers transfer and separation from OPCN catalysts to organic pollutants due to their more favorable interfacial contact and conjugative effect, resulting in superior photodegradation performances.

3.2. Photochemical properties of different photocatalysts

For the obtained OPCN, narrowed band gaps and improved light-harvesting capacity have been achieved. To explore the impacts of these alterations on photoelectric activities thoroughly, PL spectra, photocurrent responses and EIS tests were employed jointly. A strong PL emission peak at approximately 470 nm could be found for g-C₃N₄ under excitation wavelength $\lambda = 350$ nm (Fig. 5A), originating from the band-to-band recombination of electron-hole pairs. Surprisingly, the peak intensity for OPCN reduced dramatically upon AO treatment, especially for OPCN-1, which hinted that the recombination of photo-induced carriers was effectively restrained. The great suppression of energy losses was crucial to efficient photocatalytic reactions.

Apart from that, transient photocurrent responses (Fig. 5B) demonstrated that photogenerated electron density of different catalysts followed the order of OPCN-1 > OPCN-2 > OPCN-0.5 > OPCN-0.3. The EIS spectra of these samples (Fig. 5C) showed a similar tendency,

among which OPCN-1 owned the lowest resistance in the electron transport process. Based on these results, the porous structure and doped O atoms with high electronegativity enhanced the conductivity of OPCN catalysts to accelerate the transfer of photogenerated carriers from bulk to surface, thus resulting in enhanced photocatalytic activities. However, redundant O atoms might serve as recombination centers, leading to lower quantum efficiency [36].

3.3. Photocatalytic performances and recyclability test

The photodegradation performances of OPCN and pure g-C₃N₄ were examined by degradation of BPA in aqueous suspension under visible light irradiation ($420 \text{ nm} \leq \lambda \leq 780 \text{ nm}$) after the adsorption-desorption equilibrium was reached in darkness (Fig. 6A). The influence of adsorption and photolysis on BPA might be neglected due to controlled experiments, and only 38% of BPA was degraded within 50 min in the case of g-C₃N₄ upon being illuminated by visible light. However, OPCN catalysts could efficiently oxidize BPA with enhanced photodegradation activities in the order of OPCN-1 (99%) > OPCN-2 (88%) > OPCN-0.5 (75%) > OPCN-0.3 (73%). Obviously, the content of dopants in g-C₃N₄ had a great effect on its catalytic activity in the heterogeneous photocatalytic system [33,34]. An appropriate concentration of O atoms in g-C₃N₄ not only expanded its visible light response, but also modulated the energy level well, which was beneficial to the superior photoelectrochemical activity and thus improved the photocatalytic performance. Conversely, excessive O atoms readily acted as recombination

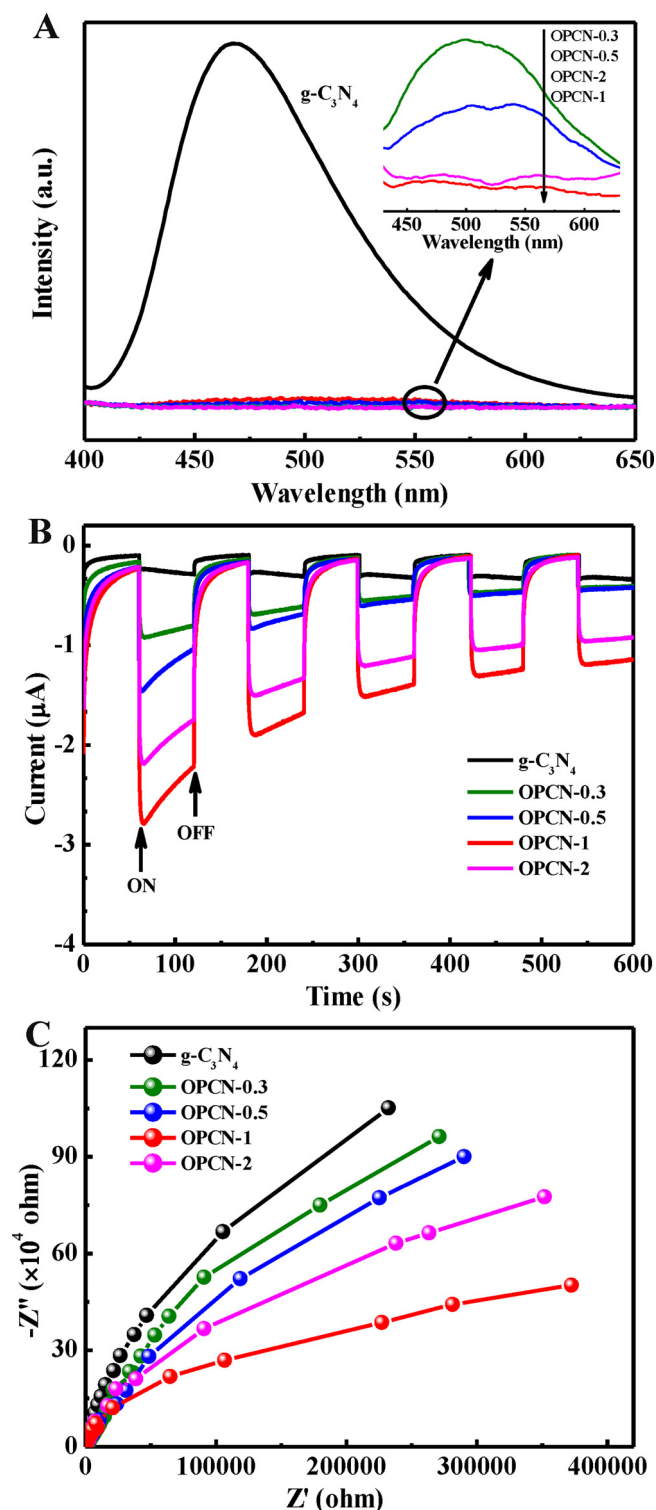


Fig. 5. (A) PL spectra (excitation wavelength $\lambda = 350$ nm), (B) time dependent photocurrent responses and (C) EIS Nyquist plots of g-C₃N₄ and OPCN.

centers for g-C₃N₄, hindering these photocatalytic processes. These BPA photodegradation reactions followed first-order kinetics closely (Fig. 6B). The apparent reaction rate constants (k) were computed to be 0.011, 0.012, 0.035 and 0.018 min⁻¹ from OPCN-0.3 to OPCN-2, respectively, which were almost 3–9 times faster than pure g-C₃N₄ (0.004 min⁻¹). Moreover, after 50 min irradiation, much higher mineralization rates of OPCN-0.3 (46%), OPCN-0.5 (42%), OPCN-1 (75%) and OPCN-2 (60%) were observed in comparison with g-C₃N₄ (23%)

(Fig. 6C). These phenomena suggested that the higher removal effect and mineralization ability were achieved for modified OPCN catalysts.

Furthermore, it was readily observed that the photodegradation rate of g-C₃N₄ for BPA removal increased more significantly under simulated solar irradiation than visible light irradiation (Fig. S6A), while almost no changes were found for OPCN-1 under both conditions. Accordingly, it could be speculated that the photocatalytic performances of OPCN were mainly induced by visible light irradiation, which resulted from O doping and led to the reduction of energy consumption. Moreover, the required times for complete degradation of various organic pollutants were 30 min for RhB, 60 min for 2-CP and 2,4,6-TCP, 90 min for phenol and 2,4-DCP, and 120 min for MB and MO in OPCN-1 suspensions with visible light irradiation (Fig. S6B). These results verified that OPCN catalysts were effective broad-spectrum visible-light photocatalysts. The efficient separation and fast migration of photoinduced charge carriers led to superior photocatalytic activities. Meanwhile, cycling tests (Fig. 6D) exhibited no significant loss of photoactivity for BPA removal after five cycles under the same conditions. The XRD patterns of OPCN-1 before and after cycling tests were almost identical (Fig. S7), affirming the excellent photostability and reutilization of OPCN. In summary, OPCN photocatalysts were successfully prepared by introducing O atoms with a low cost but efficient activity and high stability, displaying excellent potential for the photooxidation elimination of persistent organic pollutants.

3.4. Mechanism of enhanced photodegradation activity

To ascertain the photocatalytic mechanism for the oxidation of organic contaminants over OPCN samples under visible light irradiation, effects of different radical scavengers on BPA degradation over OPCN-1 were determined in Fig. 7A. No obvious effect on the photoactivity was observed when tert-butyl alcohol (t-BA, $\cdot\text{OH}$) was added, while only 69% of BPA was eliminated within 50 min after the addition of Na₂C₂O₄ (h^+). Astonishingly, BPA removal was significantly restrained after being degassed with N₂ to exhaust O₂, suggesting that O₂ \cdot^- played major role in this photocatalytic system. Furthermore, the ESR technique with BMPO was also carried out to test the generation of O₂ \cdot^- and $\cdot\text{OH}$ (Fig. 7B and S8). No characteristic peaks of BMPO-O₂ \cdot^- were observed for either g-C₃N₄ or OPCN-1 in the condition of darkness. Excitingly, once illuminated by visible light, the signals of BMPO-O₂ \cdot^- emerged immediately, and its intensity for OPCN-1 was much stronger than that of g-C₃N₄. This hinted that O doping benefited the yield of O₂ \cdot^- radicals in the OPCN-1 photocatalytic system. Meanwhile, $\cdot\text{OH}$ radicals were not detected in g-C₃N₄ and OPCN-1 suspensions in the dark or under visible light irradiation. Based on radical trapping and ESR results, O₂ \cdot^- radicals and excited h^+ were primarily responsible for organic pollutants removal over OPCN, which were generated as in the following equations:



Accordingly, photodegradation of BPA over catalysts was a multi-step pathway, which mainly depended on intrinsic properties of these materials. The previous theoretical study has shown that such a photodegradation reaction was mainly induced by holes and that the main electrophilic sites were located at the C4 or C10 atom of BPA, as labeled in the structure in Fig. 8A. Motivated by their work, we explored the photodegradation of BPA at the C4 atom attacking center over OPCN. For OPCN, Bader charge analysis found that most hole carriers gathered on the N2' atom. Herein, we selected the N2' atom as the preferred active site to attack BPA during degradation processes, which was noted as the OPCN_N⁺-BPA pathway in Fig. 8B. Moreover, the uniquely doped O atoms in OPCN were also chosen as alternative active sites to attack BPA molecules due to their strong reactivity (defined as the OPCN_O⁺-BPA pathway in Fig. 8C) [37,38].

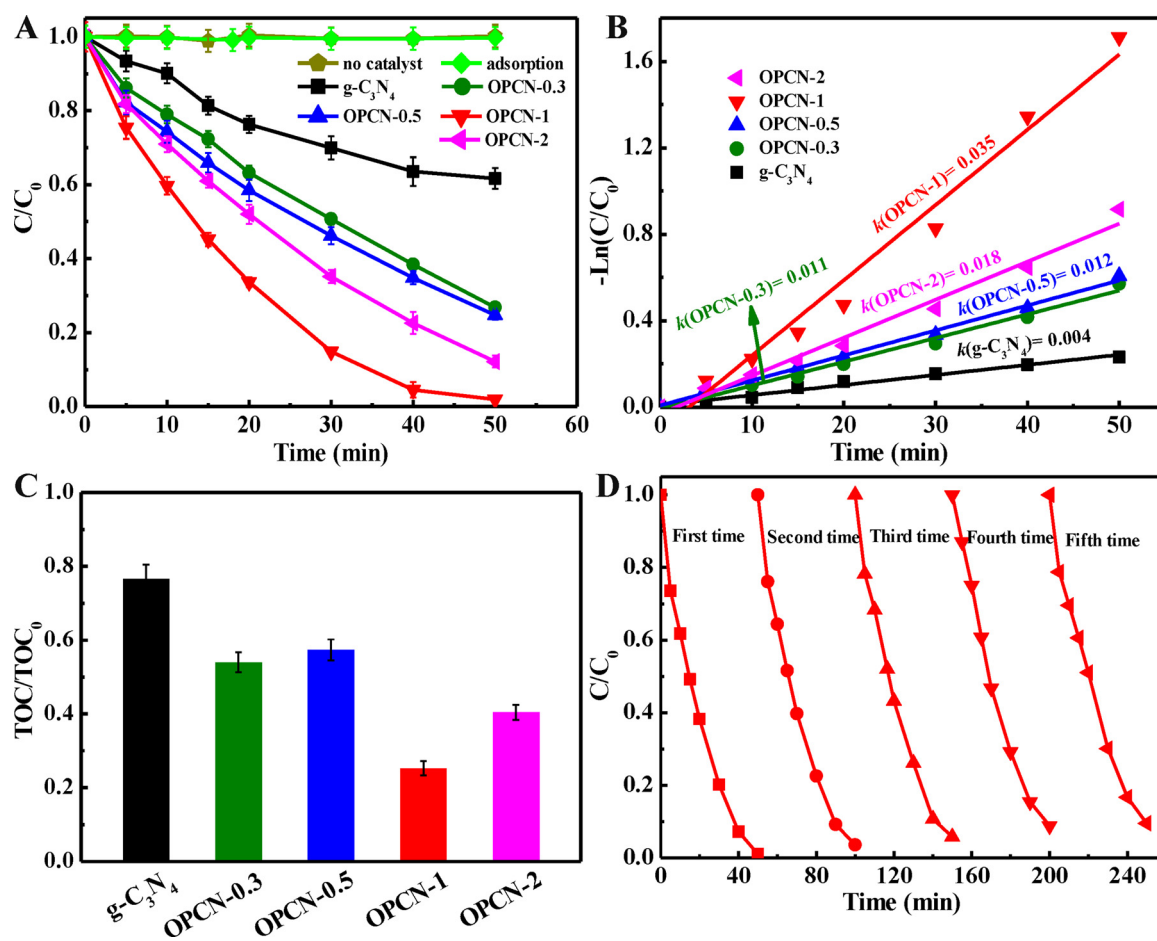


Fig. 6. (A) Photocatalytic degradation of BPA over pure $g-C_3N_4$ and OPCN samples under visible light irradiation ($420 \text{ nm} \leq \lambda \leq 780 \text{ nm}$), (B) the corresponding pseudo-first-order reaction kinetic fitted curves, (C) TOC removal rates for different catalysts, and (D) cycling runs of BPA degradation over OPCN-1 suspensions.

In the OPCN_N^+ -BPA pathway (Fig. 8B), the OPCN_N^+ first attacked the C4 of BPA and formed the intermediate product “int1” with an N–C distance of 1.553 \AA . This was the rate-determining step, which had an activation energy of $68.43 \text{ kcal mol}^{-1}$ as calculated at the PBE1PBE level. Subsequently, the next step should be the C4–C1 breakage assisted by OPCN. However, we finally obtained a product with linked C8–C11 bond, although the C4–C1 distance was separated by 3.353 \AA . We then considered the other degradation channel which included the participation of $\text{O}_2^{\cdot-}$ radicals. After injection of $\text{O}_2^{\cdot-}$, the C–C bond was broken from 1.570 \AA to 4.345 \AA after overcoming a free energy barrier of $48.44 \text{ kcal mol}^{-1}$. Thus far, the BPA molecule was split into two

molecular fragments by OPCN.

For the other OPCN_O^+ -BPA degradation pathway (Fig. 8C), the first reaction coordinate was the distance between the C4 and O atoms. OPCN_O^+ gradually approached the BPA molecule with the C4–O distance shortened from 3.863 \AA to 1.454 \AA . During this process, an intermediate with a five-membered ring (int1) was formed by passing a transition state TS1 whose O–C bond length and free energy barrier were 1.987 \AA and $96.44 \text{ kcal mol}^{-1}$, respectively. The C4–C1 bond of BPA was then changed from 1.572 \AA (int) to 2.572 \AA (P) via TS2 whose relative energy decreased to $14.40 \text{ kcal mol}^{-1}$, and the BPA molecule was separated into two fragments. On the basis of the above results, we

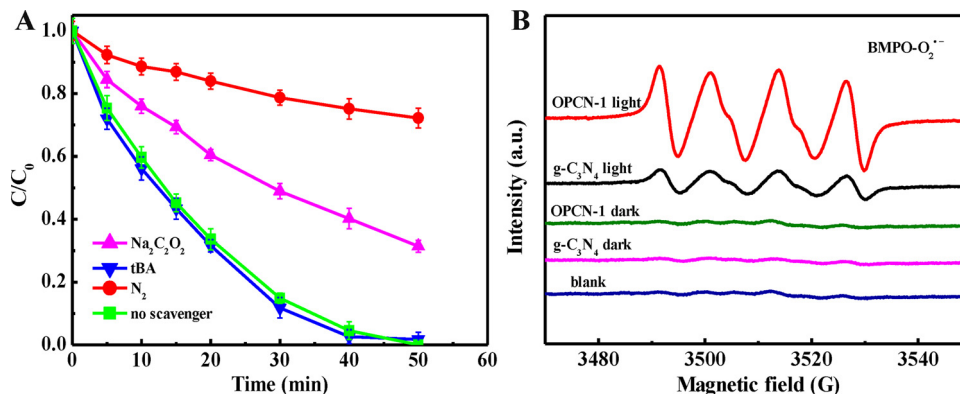


Fig. 7. (A) Effect of different radical scavengers on photodegradation of BPA over OPCN-1, and (B) BMPO spin-trapping ESR spectra of catalysts in methanol dispersion for $\text{BMPO-O}_2^{\cdot-}$.

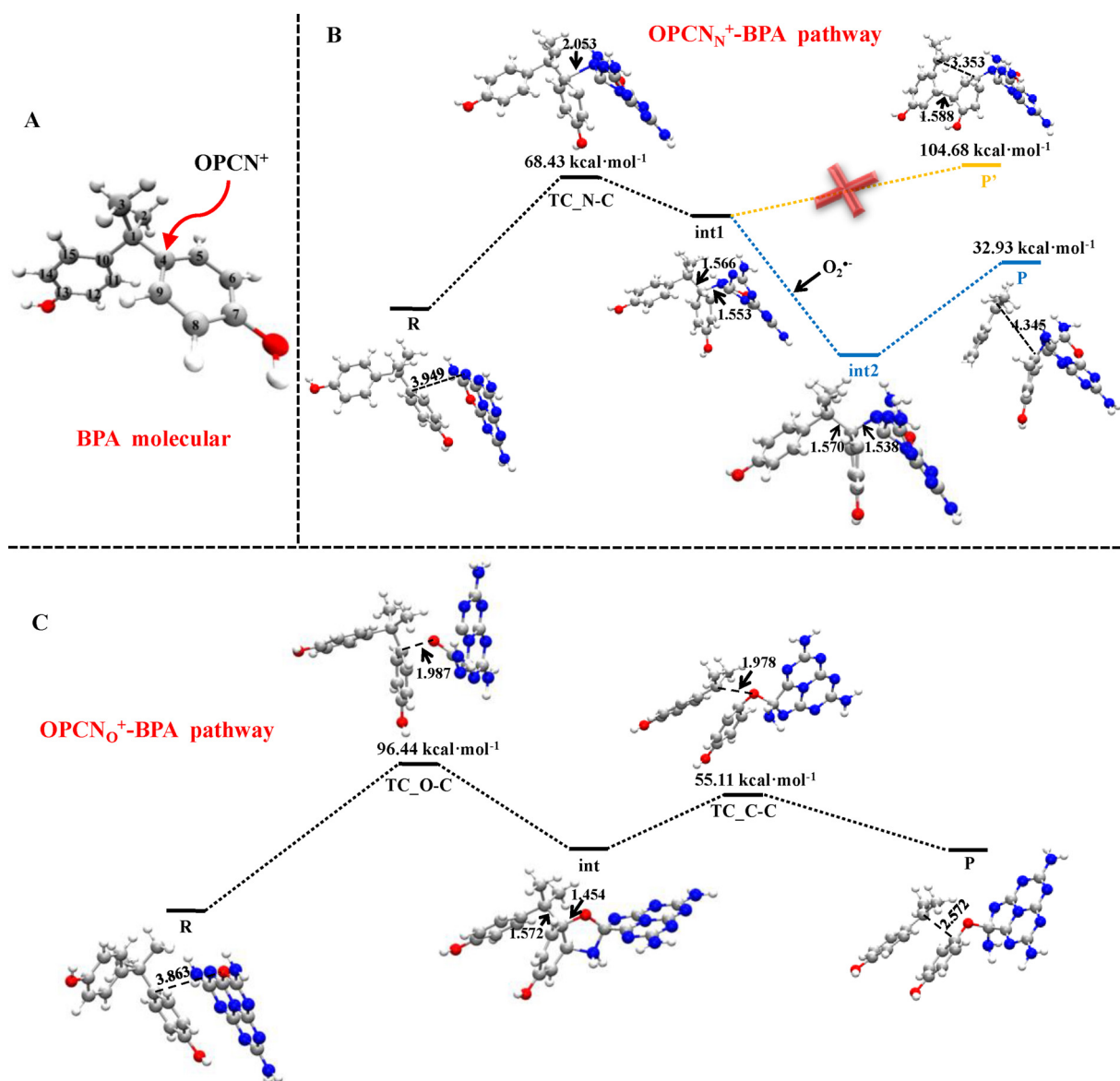


Fig. 8. (A) The active sites of BPA for OPCN attacks. DFT calculated structures of reactants, intermediates and transition state for the degradation of BPA attacked by OPCN catalysts with (B) N atoms or (C) doped O atoms as reactive sites (white, red, gray and blue balls represented H, O, C and N elements, respectively) (For interpretation of the references to colour in this figure legend, the reader is referred to the web version of this article).

further calculated potential energy surfaces of excited states along these two pathways, as shown in Fig. S9. It was found that profiles in the excited state displayed the same trend as those in the ground state. As a result, OPCN catalysts could serve as effective carriers for photo-generated h^+ , which presented crucial effects on inducing degradation of BPA under visible light irradiation.

According to the above experimental and DFT studies, a tentative photodegradation mechanism of BPA over OPCN was depicted in Fig. 9. Once excited by visible light, photogenerated e^- transferred from the VB to the CB of OPCN and formed a conjugated delocalized π system, which then rapidly reduced O_2 on the surface of catalysts to yield $O_2^{\cdot-}$, owing to their more negative CB potentials (-0.85 - -0.93 eV) versus the reduction potential of $O_2/O_2^{\cdot-}$ (-0.33 eV vs. NHE) [16,39]. These $O_2^{\cdot-}$ radicals would mineralize BPA directly into CO_2 and H_2O due to their strong oxidation power [40]. However, the VB potentials of these samples (+0.95 - +1.17 eV) were much less positive than the standard redox potential of $OH^-/^{\cdot}OH$ (+2.38 eV vs. NHE) [41], so that h^+ left on the VB of OPCN could not oxidize OH^- to produce $^{\cdot}OH$ kinetically. Actually, the gathered h^+ could easily trigger the reactions at the

beginning by attacking BPA molecules and separating them into small molecules, as in the OPCN_N⁺-BPA and OPCN_O⁺-BPA pathways. Subsequently, $O_2^{\cdot-}$ radicals further participated in these degradation reactions and decomposed intermediate products into CO_2 and H_2O [40,42]. Therefore, potential energy levels and porous structure built by O doping contributed to higher light adsorption ability and light quantum efficiencies, leading to the generation of more active species and enhanced photocatalytic activities.

4. Conclusion

In summary, we successfully fabricated novel dual-O-doped porous g-C₃N₄ photocatalysts via thermal condensation with urea and AO as precursors. Bi-substituted O doping for N atoms (in the para-positions, N1' and N4' sites) and porous structure were fabricated mainly by activation of AO molecules, resulting in the enlarged specific surface area, narrowed band gap and expanded visible light response. Consequently, photodegradation activity of the optimal OPCN was enhanced by nearly 9 times versus g-C₃N₄ under ambient conditions. Combined with

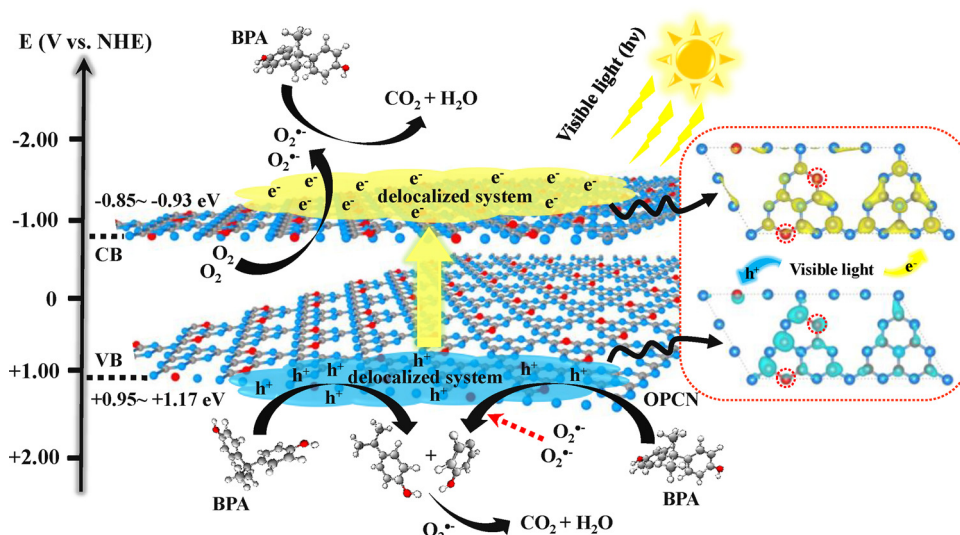


Fig. 9. Proposed photodegradation mechanism for BPA in aqueous solution by OPCN under visible light irradiation (white, red, gray and blue balls represented H, O, C and N elements, respectively) (For interpretation of the references to colour in this figure legend, the reader is referred to the web version of this article).

experimental and theoretical information, it was found that O doping led to effective charge transfer and separation of OPCN by forming surface e^- and h^+ -related conjugated delocalized systems under visible light irradiation, which benefited its interfacial contact to organic pollutants and adsorbed O_2 . As a result, the degradation of BPA was easily induced by photogenerated h^+ and then thoroughly mineralized by $O_2^{\bullet-}$. On the other hand, more $O_2^{\bullet-}$ radicals were yielded, which could also oxidize BPA directly due to their strong oxidation power. Thus, reassembly of g-C₃N₄ by doping a nonmetallic element with stronger electronegativity than C provides a promising approach to fabricate highly effective nonmetal photocatalysts for wastewater treatment.

Acknowledgments

This work was supported by the National Key Research and Development Program of China (2017YFA0207002), NSFC (21836001, 21607042, 21707033, 21777,039 and 21577,032), and the Fundamental Research Funds for the Central Universities (2017MS045, 2017YQ001 and 2018ZD11). X. Wang acknowledged the CAS Interdisciplinary Innovation Team of Chinese Academy of Sciences.

Appendix A. Supplementary data

Supplementary material related to this article can be found, in the online version, at doi:<https://doi.org/10.1016/j.apcatb.2019.02.008>.

References

- N. Liu, W.Y. Huang, M.Q. Tang, C.C. Yin, B. Gao, Z.M. Li, L. Tang, J.Q. Lei, L.F. Cui, X.D. Zhang, *Chem. Eng. J.* (2018), <https://doi.org/10.1016/j.cej.2018.11.143>.
- W.Y. Huang, N. Liu, X.D. Zhang, M.H. Wu, L. Tang, *Appl. Surf. Sci.* 425 (2017) 107–116.
- T.Q. Wang, Z.F. Jiang, T.C. An, G.Y. Li, H.J. Zhao, P.K. Wong, *Environ. Sci. Technol.* 52 (2018) 4774–4784.
- H. Li, H. Shang, X.M. Cao, Z.P. Yang, Z.H. Ai, L.Z. Zhang, *Environ. Sci. Technol.* 52 (2018) 8659–8665.
- R. Ma, S. Zhang, T. Wen, P.C. Gu, L. Li, G.X. Zhao, F.L. Niu, Q.F. Huang, Z.W. Tang, X.K. Wang, *Catal. Today* (2018), <https://doi.org/10.1016/j.cattod.2018.11.016>.
- U. Banin, Y. Ben-Shahar, K. Vinokurov, *Chem. Mater.* 26 (2013) 97–110.
- X.D. Zhang, Y. Yang, W.Y. Huang, Y.Q. Yang, Y.X. Wang, C. He, N. Liu, M.H. Wu, L. Tang, *Mater. Res. Bull.* 99 (2018) 349–358.
- S. Zhang, P.C. Gu, R. Ma, C.T. Luo, T. Wen, G.X. Zhao, W.C. Cheng, X.K. Wang, *Catal. Today* (2018), <https://doi.org/10.1016/j.cattod.2018.09.013>.
- J. Wang, Z. Yang, X.X. Gao, W.Q. Yao, W.Q. Wei, X.J. Chen, R.L. Zong, Y.F. Zhu, *Appl. Catal. B Environ.* 217 (2017) 169–180.
- X.J. Zou, Y.Y. Dong, Z.B. Chen, D.P. Dong, D.X. Hu, X.Y. Li, Y.B. Cui, *RSC Adv.* 6 (2016) 20664–20670.
- T. Xiong, W.L. Cen, Y.X. Zhang, F. Dong, *ACS Catal.* 6 (2016) 2462–2472.
- X.S. Rong, F.X. Qiu, J. Rong, X.L. Zhu, J. Yan, D.Y. Yang, *Mater. Lett.* 164 (2016) 127–131.
- L.B. Jiang, X.Z. Yuan, G.M. Zeng, X.H. Chen, Z.B. Wu, J. Liang, J. Zhang, H. Wang, H. Wang, *ACS Sustain. Chem. Eng.* 5 (2017) 5831–5841.
- Y.Y. Wang, W.J. Yang, X.J. Chen, J. Wang, Y.F. Zhu, *Appl. Catal. B Environ.* 220 (2018) 337–347.
- Z. Sun, M. Zhu, M. Fujitsuka, A. Wang, C. Shi, T. Majima, *ACS Appl. Mater. Interfaces* 9 (2017) 30583–30590.
- Y. Shang, X. Chen, W. Liu, P. Tan, H. Chen, L. Wu, C. Ma, X. Xiong, J. Pan, *Appl. Catal. B Environ.* 204 (2017) 78–88.
- L. Xu, W.-Q. Huang, L.-L. Wang, Z.-A. Tian, W. Hu, Y. Ma, X. Wang, A. Pan, G.-F. Huang, *Chem. Mater.* 27 (2015) 1612–1621.
- J. Xue, S. Ma, Y. Zhou, Z. Zhang, M. He, *ACS Appl. Mater. Interfaces* 7 (2015) 9630–9637.
- J. Fu, B. Zhu, C. Jiang, B. Cheng, W. You, J. Yu, *Small* 13 (2017).
- K. Li, X. Xie, W. Zhang, *Chem. Catal.* 8 (2016) 2128–2135.
- H. Yang, Y. Zhou, Y. Wang, S. Hu, B. Wang, Q. Liao, H. Li, J. Bao, G. Ge, S. Jia, J. Mater. Chem. A 6 (2018) 16485–16494.
- S.C. Yan, Z.S. Li, Z.G. Zou, *Langmuir* 26 (2010) 3894–3901.
- I. Choudhuri, G. Bhattacharyya, S. Kumar, B. Pathak, J. Mater. Chem. C 4 (2016) 11530–11539.
- Q. Guo, Y. Zhang, J. Qiu, G. Dong, J. Mater. Chem. C 4 (2016) 6839–6847.
- M. Jourshabani, Z. Shariatinia, A. Badiei, J. Phys. Chem. C 121 (2017) 19239–19253.
- Z. Tong, D. Yang, Z. Li, Y. Nan, F. Ding, Y. Shen, Z. Jiang, *ACS Nano* 11 (2017) 1103–1112.
- Z.-F. Huang, J. Song, L. Pan, Z. Wang, X. Zhang, J.-J. Zou, W. Mi, X. Zhang, L. Wang, *Nano Energy* 12 (2015) 646–656.
- J. Li, B. Shen, Z. Hong, B. Lin, B. Gao, Y. Chen, *Chem. Commun.* 48 (2012) 12017–12019.
- G. Kresse, D. Joubert, *Phys. Rev. B* 59 (1999) 1758–1775.
- Y. Zhang, J. Liu, G. Wu, W. Chen, *Nanoscale* 4 (2012) 5300–5303.
- L.Q. Yang, J.F. Huang, L. Shi, L.Y. Cao, Q. Yu, Y.N. Jie, J. Fei, H.B. Ouyang, J.H. Ye, *Appl. Catal. B Environ.* 204 (2017) 335–345.
- V.W. Lau, I. Moudrakovski, T. Botari, S. Weinberger, M.B. Mesch, V. Duppel, J. Senker, V. Blum, B.V. Lotsch, *Nat. Commun.* 7 (2016) 12165–12174.
- J. Zhang, M. Zhang, R. Sun, X. Wang, *Angew. Chem. Int. Ed.* 51 (2012) 10145–10149.
- W. Yang, L. Zhang, J. Xie, X. Zhang, Q. Liu, T. Yao, S. Wei, Q. Zhang, Y. Xie, *Angew. Chem. Int. Ed.* 55 (2016) 6716–6720.
- L. Yang, X. Li, G. Zhang, P. Cui, X. Wang, X. Jiang, J. Zhao, Y. Luo, J. Jiang, *Nat. Commun.* 8 (2017) 16049.
- Q. Li, N. Zhang, Y. Yang, G. Wang, D. Ng, *Langmuir* 30 (2014) 8965–8972.
- L. Zhao, X. Xiao, L. Peng, F.L. Gu, R.Q. Zhang, *RSC Adv.* 4 (2014) 10343–10349.
- X. Zhao, P. Du, Z. Cai, T. Wang, J. Fu, W. Liu, *Environ. Pollut.* 232 (2018) 580–590.
- L.L. Zhang, Y.L. Shi, L. Wang, C. Hu, *Appl. Catal. B Environ.* 220 (2018) 118–125.
- C.Y. Wang, X. Zhang, X.N. Song, W.K. Wang, H.Q. Yu, *ACS Appl. Mater. Interfaces* 8 (2016) 5320–5326.
- H. Cheng, B. Huang, Y. Dai, X. Qin, X. Zhang, *Langmuir* 26 (2010) 6618–6624.
- J. Yuan, Q. Wu, P. Zhang, J. Yao, T. He, Y. Cao, *Environ. Sci. Technol.* 46 (2012) 2330–2336.